GDCh

**Research Article**

*Angewandte*
*Chemie*
International Edition
www.angewandte.org

**Carbon Electrodes**

# Unlocking Mesoscopic Disorder in Graphitic Carbon with Spectroelectrochemistry

*Ry Papadopoulos[+], Benjamin Masters[+], Arpan Kundu[+], Nicholas Maldonado, Alexander S. Filatov, Yuzi Liu, Taemin Kim, Giulia Galli, and Anna Wuttig\**

**Abstract:** Intrinsic structural and oxidic defects activate graphitic carbon electrodes towards electrochemical reactions underpinning energy conversion and storage technologies. Yet, these defects can also disrupt the long-range and periodic arrangement of carbon atoms, thus, the characterization of graphitic carbon electrodes necessitates *in-situ* atomistic differentiation of graphitic regions from mesoscopic bulk disorder. Here, we leverage the combined techniques of *in-situ* attenuated total reflectance infrared spectroscopy and first-principles calculations to reveal that graphitic carbon electrodes exhibit electric-field dependent infrared activity that is sensitive to the bulk mesoscopic intrinsic disorder. With this platform, we identify graphitic regions from amorphous domains by discovering that they demonstrate opposing electric-field-dependent infrared activity under electrochemical conditions. Our work provides a roadmap for identifying mesoscopic disorder in bulk carbon materials under potential bias.

## Introduction

Graphitic carbon materials serve as a ubiquitous electrode material class in energy conversion and storage devices due to their scalability, durability, conductivity, and wide electro-chemical potential window. The intrinsic oxidic and structural disorder known to form under polarization bias and aqueous conditions[1] activates graphitic carbon towards electrochemical reactions that underpin these technologies.[2,3] For example, *ex-situ* characterization in concert with computational models have led to the hypothesis that topological defects,[4,5] edges,[6–9] or sites adjacent to or at oxygen-defects[9,10] can serve as active sites for the oxygen reduction reaction.[11] Similarly, these combined tools suggest that carbon atoms around pentagonal and octagonal structures or zig-zag and armchair edges enable $CO_2$ electroreduction.[12,13] These microscopic defects can also introduce mesoscopic disorder, i.e., amorphous domains, by disrupting the long-range and periodic arrangement of carbon atoms.[14–16] The centrality of intrinsic defects and their emerging role in activating electrochemical reactions at scalable and low-cost carbon electrodes necessitates the development of *in-situ* spectroscopic tools and computational models that identify the intrinsic mesoscopic disorder.

Vibrational spectroscopy of bulk graphite characterizes the structure of the $sp^2$ building block under applied potentials in a non-destructive fashion. In Raman spectroscopy, the introduction of disorder activates the $A_{1g}$ breathing mode near 1355 cm$^{-1}$ (D peak), which is forbidden in crystalline graphite.[17–19] The phonon linewidth and intensity of this feature relative to the $E_{2g(2)}$ in-plane vibrational mode at 1580–1600 cm$^{-1}$ (G peak) present in crystalline graphite has been related to the degree of disorder (i.e., the clustering of the $sp^2$ phase, changes in C–C bond angles and lengths, the $sp^2$:$sp^3$ ratio, and the presence of $sp^2$ rings or chains).[18,20–22] The ability to track the potential-dependence of the D band has revealed how graphitic carbon electrodes restructure under electrochemical conditions; for example, Raman experiments have revealed the formation of structural defects and delamination following oxidation[23,24] and the presence of disorder in the $sp^2$ lattice during electrolyte ion intercalation.[25–28] However, changes in the D band do not distinguish between amorphous regions and intrinsic oxidic defects. Infrared spectroscopy (IR) offers a complementary, non-destructive approach to characterize graphitic carbon *in-situ*. The effects of disorder on the known IR-active $A_{2u}$ mode at 868 cm$^{-1}$ and $E_{1u}$ mode at 1588 cm$^{-1}$ of crystalline graphite[29–31] and their changes under applied potential remain open questions; however, oxygen motifs exhibit varying dipole moments that can be tracked using IR spectroscopy.[32–36] Thus, we hypothesized that IR spectroscopy combined with computational models presents an *in-*

[*] R. Papadopoulos,[+] B. Masters,[+] Dr. A. Kundu,[+] N. Maldonado,
Dr. A. S. Filatov, T. Kim, Prof. G. Galli, Prof. A. Wuttig
Department of Chemistry
University of Chicago
Chicago, IL 60637, United States
E-mail: awuttig@uchicago.edu

Dr. A. Kundu,[+] Prof. G. Galli
Pritzker School of Molecular Engineering
University of Chicago
Chicago, IL 60637, United States

Dr. Y. Liu, Prof. G. Galli
Argonne National Laboratory
Lemont, IL 60439, United States

[+] These authors contributed equally to this work.

*situ* strategy to characterize amorphous domains, graphitic regions, and oxygen defects in bulk graphitic carbon.

Here, we prepare graphitic and disordered carbon electrodes compatible with *in-situ* IR and computational modeling. We deposit a continuous film of disordered graphitic carbon material, specifically, reduced graphite oxide (rGO), onto conductive and high-refractive index substrates,[36,37] which enables their subsequent *in-situ* characterization by attenuated total reflectance (ATR)-IR. We employ first-principles calculations of *in-silico* constructed bulk rGO models that capture the incorporation of *ex-situ* experimentally observed oxidic defects, graphitic domains, and amorphous regions at the atomic level. By probing the *in-situ* ATR-IR spectra of the rGO electrodes under applied potential bias, we discover two IR-active features that exhibit opposing potential-dependent IR activities (Stark shifts) in aqueous electrolytes. Using our first-principles calculations of *in-silico* constructed bulk rGO models, we reveal disparate vibrational Stark effects in graphitic regions and intrinsic mesoscopic disorder. Thus, our work demonstrates that ATR-IR combined with theoretical models facilitates the identification of mesoscopic disorder in bulk graphitic carbon electrodes *in-situ*.

## Results and Discussion

*Ex-situ* characterization data are in line with the formation of a disordered rGO film following electroreduction from GO. rGO was electrodeposited on Au-coated Si substrates (Au/Si) compatible with ATR-IR (all synthesis procedures detailed in the Supporting Information and in Figures S1–

S4). X-ray photoelectron spectroscopy (XPS) data are consistent with the formation of a rGO film on Au surfaces. Figure 1a depicts the high-resolution C 1s XPS data of the resulting film. In contrast to the GO dropcast on Au (Figures S5a and S6a), we observe a significant decrease in the peak centered at 286.4 eV, attributed to ether and hydroxyl moieties (C–O–C/C–OH) with contributions from carbonyl (C=O) and carboxylic acid ((C=O)OH) moieties.[38,39] The IR spectrum of the GO precursor compared with that obtained for rGO similarly shows a significant decrease in C–O–C, C–OH, C=O, and carboxylic acid (C=O)OH functionalities (Figures S7 and S8, Tables S1 and S2), in line with XPS results. Furthermore, the high-resolution O 1s XPS data of the rGO film show an absolute decrease in all oxidic functionalities compared to GO (Figures S5b, S6b, and S9). An analysis of the relative peak area ratios of the C 1s and O 1s XPS features of the rGO film suggests a 14% atomic oxygen surface (Figure S10), a significant reduction from the 39% value observed for GO dropcast on Au (Figure S11, Table S3). In addition, in contrast to the GO dropcast on Au (Figures S5a, S6a, S10, S11), we observe an increase in the peak centered at 284.6 eV for the electrodeposited rGO shown in Figure 1a, primarily attributed to carbon in disordered regions, i.e., $sp^3$ carbon, vacancies, edges, pentagons, and heptagons ($C_{disorder}$),[38] and carbons bound to oxidized carbons ($C–C_{oxidized}$).[39,40] We note that crystalline graphite, with negligible disorder, is well-documented to exhibit a feature at 283.3 eV ($Csp^2$), demonstrating that the $C_{disorder}$ peak observed here encompasses $sp^2$ carbons with binding energies positively shifted from the expected 283.3 eV value due to the introduction of disorder.[38] The Au 4f XPS region of
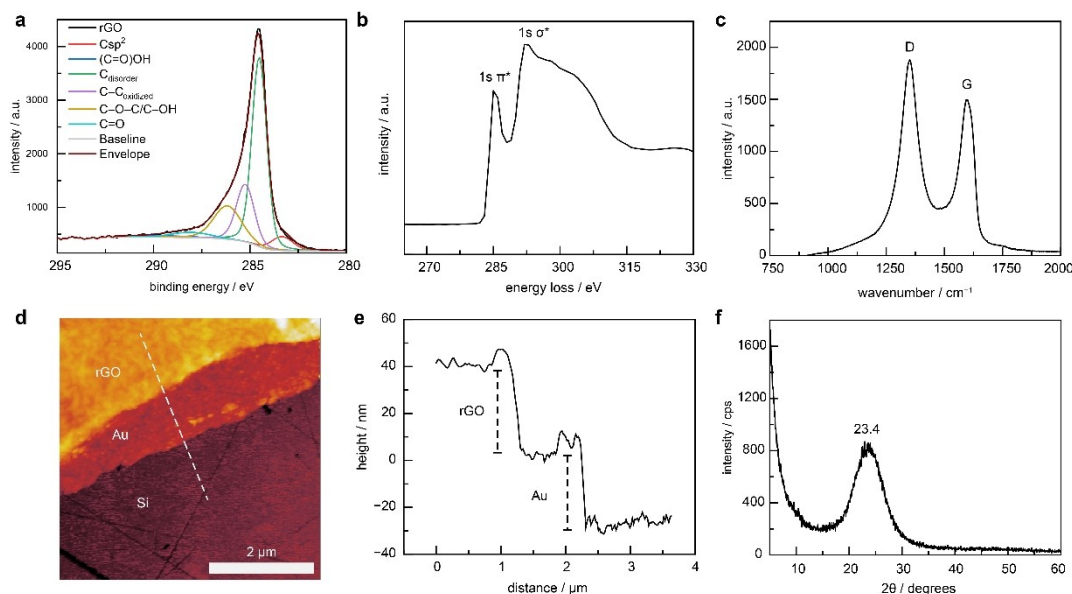


**Figure 1.** Characterization of reduced graphite oxide (rGO) films prepared via the electrodeposition of GO on Au-coated Si (Au/Si) surfaces. (**a**) High-resolution x-ray photoelectron spectra of the C1s region. (**b**) Electron energy-loss spectra of carbon K-edges. (**c**) Raman spectrum. (**d**) Atomic force microscopy image of the rGO–Au-Si boundary and (**e**) the height profile along the dotted white line. (**f**) Grazing-incidence XRD (GIXRD). GIXRD was conducted on a 0.3 μm-thick rGO electrodeposited on Au-coated aluminosilicate glass (see Supporting Information for details).

the rGO film shows a nearly featureless spectrum, suggesting that the electrodeposited and reduced carbon film is formed with negligible Au pinholes (Figure S10, Table S4). The uniformity of the film is further supported by a featureless voltammetric profile of the resultant rGO film obtained in $N_2$-saturated 0.1 M sodium phosphate (pH 7.4); the profile is nearly identical to that observed using a glassy carbon electrode and inconsistent with Au-catalyzed hydrogen evolution reaction (HER, Figure S3), suggesting a suppression of HER over the potential range examined.

Electron energy-loss spectra (EELS) of rGO K-edges reveal a peak at 285.5 eV (Figures 1b and S12), corresponding to $\pi^*$ electronic states for carbon atoms that support the presence of $sp^2$ carbon in the resulting film.[41,42] In addition, Raman spectra are consistent with the formation of a defect-rich graphitic material, Figure 1c. For the as-prepared rGO film, we observe peaks centered at 1351 and 1597 $cm^{-1}$, in line with previously reported ranges for the G band and D band observed for rGO, respectively (Figure S13).[43] The observation of a D band suggests the presence of disorder and defects, such as the oxygen heteroatoms observed by our XPS measurement, in addition to incomplete graphitization, topological defects, in-plane distortions, and strain.[18,44–46] Atomic force microscopy (AFM) images demonstrate the formation of a ~40 nm thick film on top of the Au surface (Figures 1d and 1e). As the thickness of GO and rGO sheets have been shown to be between 1.1 and 3.6 nm,[47] the results suggest that approximately 11 to 36 sheets of rGO, at maximum, are layered on top of the Au nanofilm. Moreover, prior work suggests that multi-layer graphene structures with more than ten layers resemble electronic and spectroscopic properties of graphite,[48,49] thus, the thickness of the films observed in this work implicate the formation of a disordered graphitic carbon bulk material on Au. Figure 1f depicts the grazing incidence x-ray diffraction (XRD) data for a thicker, 0.3-µm thick rGO film (Figure S14). This thickness was chosen to rule out broadening effects in XRD inherent to nanoscale materials. A broad peak at 23.4° was observed, corresponding to a *d*-spacing of 3.8 Å, which approaches the *d*-spacing of graphite at 3.4 Å,

in line with literature reports.[50,51] The broadness of the feature suggests that the disordered graphitic carbon film contains amorphous domains, as previously observed.[50,51] Scanning electron microscopy (SEM) images are consistent with the formation of a layered structure (Figure S15) on the electrode surface. Furthermore, in Figures S16 and S17, we demonstrate that the IR beam penetrates the rGO/Au/Si composite in an ATR configuration. The comparable IR intensities of a vibrational probe molecule (*p*-nitrobenzoic acid) on the surface of rGO/Au/Si and on bare Si suggest that the rGO/Au/Si system is compatible with ATR-IR spectroscopy for carbon material characterization. We note that the enhanced IR intensities of *p*-nitrobenzoic acid observed on the Au/Si surface relative to that observed in the presence of the rGO (i.e., rGO/Au/Si) and absence of Au (i.e., bare Si) are in line with the expected surface-enhanced infrared absorption properties of the underlying and nanostructured Au.[52–55] Although the rGO, Au, or rGO/Au layer can reduce the ATR-IR penetration depth compared to bare Si, if the rGO/Au layer attenuates the IR penetration depth to less than the composite's thickness, vibrational probes on the rGO/Au surface relative to that on bare Si would not produce comparable IR signals at similar surface concentrations of the probe. Together, our results are consistent with the development of an electrodeposition strategy that produces a continuous film of disordered graphitic carbon on top of Au/Si composites with minimal pinholes for ATR-IR analyses.

We discover that the ATR-IR data of the rGO bulk film reveal two potential-dependent features that increase in signal intensity and exhibit opposing Stark shifts upon reductive polarization in aqueous electrolytes. Figure 2a depicts the cyclic voltammogram (CV) of the rGO film prepared on Au/Si in $N_2$-purged 0.1 M $HClO_4$. Over the potential range examined, we do not observe significant Faradaic current above the double layer capacitance, suggesting that the IR spectra do not report on processes that occur as a result of charge transfer, e.g., intercalation. Figure 2b depicts the IR spectra (spectroscopic peaks summarized in Table S5) collected during the CV experi-
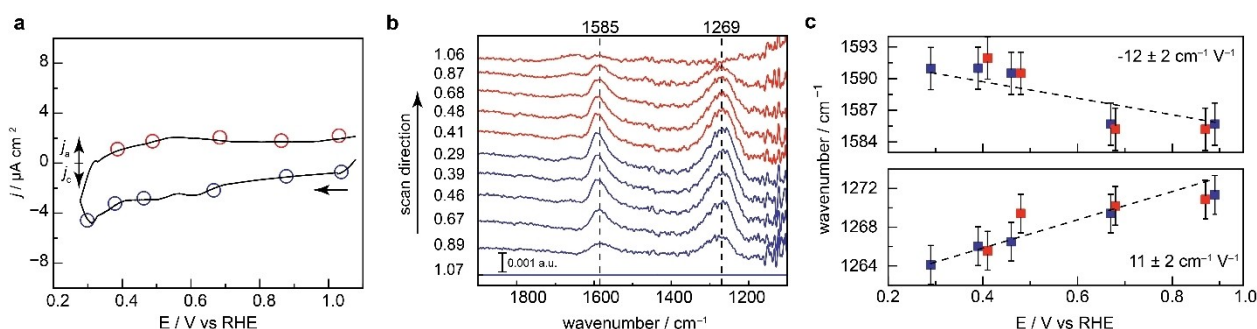


***Figure 2.*** (a) Cyclic voltammogram of reduced graphite oxide on Au/Si in 0.1 M $HClO_4$ under $N_2$-saturated conditions. Data were collected at 2 mV s$^{-1}$ with a negative direction of scan. Blue circles represent potentials where ATR-IR spectra are reported in the negative-going scan, and red circles represent potentials where ATR-IR spectra are reported in the positive-going scan in Figures 2b and 2c. (b) Simultaneously collected ATR-IR spectra during the CV scan are shown in Figure 2a. Background spectra were collected in $N_2$-saturated 0.1 M $HClO_4$ at 1.07 V vs RHE. (c) **(top)** Potential dependence of the peak position of that observed at 1585 $cm^{-1}$ at 0.89 V in Figure 2b. **(bottom)** Potential dependence of the peak position of that observed at 1269 $cm^{-1}$ at 0.89 V in Figure 2b. Error bars depict the spectral resolution.

ment, as shown in Figure 2a. At 1.07 V (all potentials quoted relative to the reversible hydrogen electrode, RHE), we observe features at 1585 and 1269 cm$^{-1}$. The intensities of the two features are reversible with respect to changes in the applied potential; they increase as the potential is driven to more negative values (from 0.89 to 0.29 V, Figure 2b, blue), and the peak intensities are diminished again once the potential is reversed at 0.29 V and driven to more oxidative values (Figure 2b, red). The peak positions of both features shift as a function of the applied potential, Figures 2c and S18. Upon reductive polarization bias, the peak at 1585 cm$^{-1}$ blueshifts to 1592 cm$^{-1}$ while the peak at 1269 cm$^{-1}$ redshifts to 1264 cm$^{-1}$. Both Stark shifts are reversible with respect to changes in the applied potential.

These features are inconsistent with IR peaks associated with the solvent or the electrolyte. Identical experiments conducted in $D_2O$ (Figure S19 and Table S6) preserve both the potential-dependent intensity changes and the peak positions, ruling out an assignment to the aqueous solvent or various protonation states of the carbon surface. We observe a shoulder at 1650–1644 cm$^{-1}$ in Figure 2b, consistent with literature reports of the bending mode of water ($\delta HOH$).[56–59] We confirm this assignment through identical experiments conducted in $N_2$-saturated 0.1 M DCl in $D_2O$, where the feature disappears and is replaced by the bending mode of $D_2O$ at 1191 cm$^{-1}$ (Figure S19 and Table S6).[60] Notably, the IR signal attributed to $\delta HOH$ in Figure 2b irreversibly increases on the CV timescale. ATR-IR spectra collected at a constant potential value (0.47 V) show an increase in the IR signal attributed to $\delta HOH$ over time (Figure S20), implicating that the growth in the water feature is dependent on time. These results suggest irreversible changes in the water population within the ATR-IR penetration depth. Notwithstanding, we do not observe the features at 1585 cm$^{-1}$ and 1269 cm$^{-1}$ for identical experiments conducted in the absence of rGO deposition (Figure S21 and Table S7), demonstrating that these features do not arise from interfacial rearrangement of the solvent or the electrolyte at the polarized Au surface. While we note that the underlying Au (Figures S16 and S17) could amplify rGO IR signals near or at the Au surface, the presence of IR peaks consistent with rGO are observed in the absence of Au (Figure S8 and Table S2) suggesting that the observed peaks in Figure 2 report on rGO structures at the Au/rGO interface as well as the bulk rGO. In addition, the features persist (Figure S22 and Table S8) for identical experiments conducted on thicker rGO films (~0.3 μm, Figure S14), consistent with their assignment to potential-dependent features associated with the bulk disordered graphitic carbon film and not the interface. Apart from the OH stretching feature of water at ~3250 cm$^{-1}$, additional features are not observed over the expanded wavenumber range observable by ATR-IR (Figure S23a). Upon conducting a second CV cycle, we observe similar peak trends (Figure S23b), indicating that the observed IR features do not arise from an irreversible modification of the rGO. We note that prior works elucidating the reduction mechanism of GO to rGO using *in-situ* polarization modulation IR reflection absorption spectroscopy observe broad features at

~1580 cm$^{-1}$ and ~1270 cm$^{-1}$, among others;[36] however, these studies do not comment on the potential-dependent changes in IR peak positions. Together, our *in-situ* spectroelectrochemical data reveal two reversible potential-dependent IR peaks, with opposing Stark effects, that are consistent with assignments to the *bulk* rGO film.

To investigate the hypothesis that a Stark effect can be observed for IR-active modes in bulk disordered graphitic carbon, we conduct first principles (FP) simulations based on density functional theory (DFT).[61–64] We consider a film of disordered carbon represented by a 128-atom supercell containing a small proportion of oxygen atoms. In contrast to prior computational structural models using molecular clusters to mimic structural motifs and investigate the IR activity of oxidized 2D carbon materials,[32–35,65] the FP calculations used here enable the incorporation of disorder in the *bulk* at the atomic level.[66,67] We carried out simulations in the presence of a finite electric field,[68,69] and we predicted IR spectra for bulk samples. Using first-principles molecular dynamics (FPMD) and an annealing-and-quenching procedure, we prepared amorphous graphitic models ($C_{114}O_{10}H_4$) that incorporate 9% atomic oxygen in the bulk via *in-silico* thermal annealing (computational details in the SI).

Figure 3a depicts one resultant model obtained at 1000 K (model-1). Model-1, which has 4 graphitic layers in the unit cell, exhibits oxygen defects in three predominant environments: phenolic (1), ether (2), and fused ether (3). Model-1 has near 100% sp$^2$ carbon content and an average inter-layer distance of 3.4 Å. Importantly, this model shows key features observed experimentally: (1) the oxygen defect amount (~9%) similar to that experimentally observed by XPS (Figures 1a and S10, Table S3); (2) the phenolic and ethereal oxygen defects observed by XPS (Figures 1a and S9); (3) the layered graphitic structure responsible for an observed *d*-spacing by XRD (Figure 1f) and further confirmed by SEM (Figure S15) and EELS (Figures 1b and S12); and (4) the amorphous nature of the material that disrupts long-range periodicity of graphitic domains giving rise to the broad XRD feature (Figure 1f). We note that the choice of the annealing temperature is important to generate models consistent with the experiments. We also generated two additional $C_{114}O_{10}H_4$ models (named Model-2 and Model-3, see SI) with varying degrees of disorder by increasing the annealing temperature (Figure S24). Although the atomistic structure of Model-2 presented several characteristics similar to the experiments, for technical reasons, we could not apply an electric field to this model as it has a close to zero band gap.[68] We found that Model-3 does not retain the layered graphitic structure observed experimentally, i.e., it is highly amorphous (71% sp$^2$ carbon). Thus, we primarily focus on Model-1 ($C_{114}O_{10}H_4$, Figure 3a), which effectively captures several key bulk properties of the experimentally probed rGO bulk film. We note that the computational methods used herein to predict the presence of a vibrational Stark effect are generalizable to materials that exhibit a band gap, and thus, these methods can be used to characterize other bulk carbon materials.
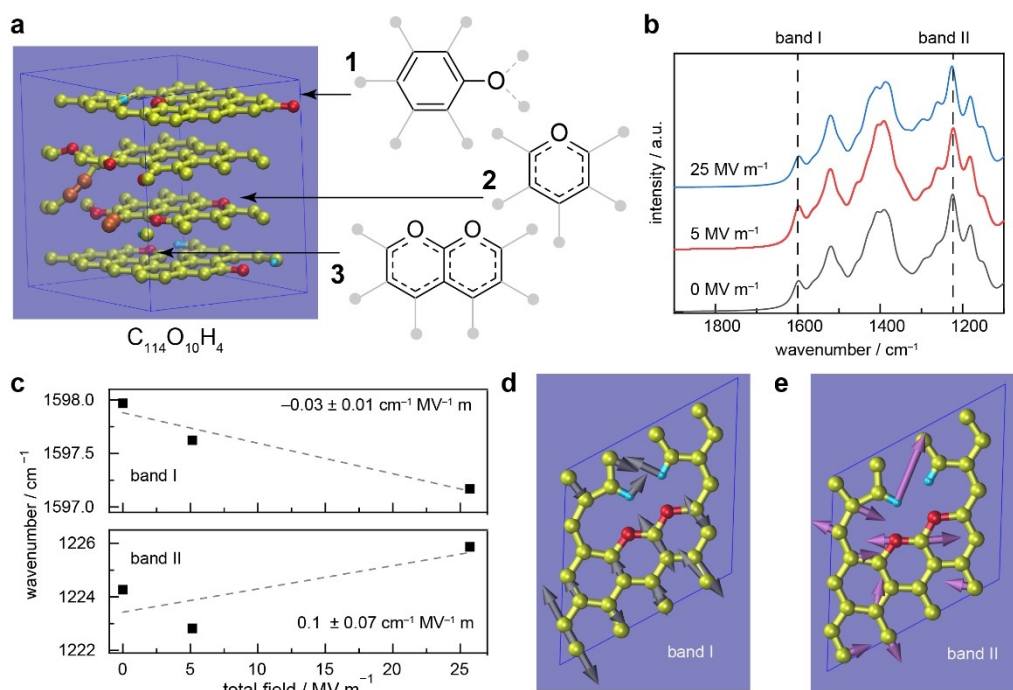
**Figure 3.** (a) Computational model-1 of bulk reduced graphite oxide with amorphous domains ($C_{114}O_{10}H_4$) and varying oxidic domains shown. Orange and yellow spheres represent $sp^2$- and sp-hybridized C atoms, red spheres represent O atoms, and cyan spheres represent H atoms. (b) Computed IR spectra of $C_{114}O_{10}H_4$ as a function of the applied field. (c) Stark shifts observed for two predominant modes along the z-axis. (d and e) Vibrational modes (only the lowest (L) layer in Figure 3a is shown) contributing to band I and band II, respectively. Other layers depict C–C displacements (see SI).

The calculated IR spectrum of $C_{114}O_{10}H_4$ reveals several features in the spectral regime observed in experiments and exhibits Stark effects. Figure 3b, black, depicts the calculated IR spectrum of Model-1. Primary features at 1598, 1518, 1407, 1390, 1224, and 1182 cm$^{-1}$ are observed (Table S9, Figure S25). We note that many narrow IR features are observed for $C_{114}O_{10}H_4$ while ATR-IR experiments show two broad IR bands (Figure 2b). We expect experimental rGO samples to have different bonding environments; this heterogeneity cannot be exhaustively sampled using first-principles simulations with supercells containing a few hundred atoms. Notwithstanding, the $C_{114}O_{10}H_4$ model derived here enables us to test the effects of a finite total electric field on the vibrational features of the film. In our analysis, we focus on the peaks appearing at 1598 cm$^{-1}$ and 1224 cm$^{-1}$ (band I and II, respectively), which exhibit opposite field-dependent shifts: band I exhibits a blueshift, whereas band II exhibits a redshift with decreasing total electric field (Figure 3c).

Figure 3d shows the vibrational mode of the lowest layer of graphitic Model-1 (shown in Figure 3a), where we have identified the mode giving rise to band I (we call it L-layer); this mode exhibits complex displacements primarily along the $C(sp^2)$–$C(sp^2)$ bonds. Vibrational modes associated with other layers of the model also exhibit displacements along $C(sp^2)$–$C(sp^2)$ bonds (Figure S26), while contributions from the oxidic defects are not observed in this frequency range. Importantly, both Model-1 and Model-2, where graphitic layers are present, exhibit IR features around 1598 cm$^{-1}$,

while the amorphous Model-3 does not have this feature, highlighting our assignment of the band to graphitic layered domains, rather than amorphous carbon (Figure S24 and 25). The shift of the *maximum* of a given band upon application of an electric field may stem from two different reasons:[70] (1) a shift of the vibrational frequency of the modes from which the band originates, and (2) a change in the relative intensity of the several, close vibrational modes contributing to the band, resulting in an effective shift of the position of the band maximum. We find that the former mechanism leads to a blueshift of band I in the presence of a decreasing electric field.

Figure 3e shows the vibrational mode of the L-layer of graphitic model-1 (shown in Figure 3a) for band II; unlike band I, we observe contributions to band II originating from C–O stretches of the oxidic defects, in addition to vibrational modes leading to complex displacements along $C(sp^2)$–$C(sp^2)$ bonds (i.e., stretching) and $C(sp^2)$–$C(sp^2)$–$C(sp^2)$ angles (i.e., bending). Other layers in the model also exhibit modes leading to similar complex displacements along $C(sp^2)$–$C(sp^2)$ bonds (i.e., stretching) and $C(sp^2)$–$C(sp^2)$–$C(sp^2)$ angles (i.e., bending) (Figure S26). Unlike band I, we do not observe any significant changes in the frequencies of the individual vibrational modes contributing to band II when an electric field is applied. Instead, the peak position shifts due to changes in the relative intensities, i.e., oscillator strengths (transition dipole moments), of the modes contributing to the peak, which correspond to $C(sp^2)$–$C(sp^2)$ bonds, $C(sp^2)$–$C(sp^2)$–$C(sp^2)$ angles, and C–O

stretches (Figure S26). Interestingly, amorphous Model-3 also exhibits IR modes at 1231 and 1291 $cm^{-1}$ with contributions from $C(sp^n)$–$C(sp^n)$ bonds (i.e., stretching) and $C(sp^n)$–$C(sp^n)$–$C(sp^n)$ angles (i.e., bending), where n equals 2 or 3 due to the amorphous structure with higher $sp^3$ content (Figure S27). In this amorphous model, the IR peaks in this spectral region (1200–1300 $cm^{-1}$) similarly exhibit redshifts with decreasing electric field (Figure S28); these shifts originate from changes in the relative intensities of the modes contributing to the peak. Thus, for band II, our simulations show that graphitic Model-1 and amorphous Model-3 similarly give rise to redshifted IR features in the 1200–1300 $cm^{-1}$ region, demonstrating that these features persist irrespective of the extent of mesoscopic disorder. Importantly, in Model-3, larger electric fields can be applied (Figure S28) compared to Model-1 (Figure 3). Thus, for Model-3, the observed persistence of the redshifting IR peaks in the 1200–1300 $cm^{-1}$ region with decreasing electric field (Figure S28b) further support the field-dependent effects of band II observed in Model-1. This result differs from our assignment of band I, see above, where the graphitic model-1 gives rise to a blue-shifted IR feature in the 1600 $cm^{-1}$ region, whereas the amorphous Model-3 does not; hence, we conclude that the peak at 1600 $cm^{-1}$ pertains to graphitic domains oriented perpendicular to the simulated applied field. We note that although the small total electric field applied in our calculations does not significantly impact the positions of the valence band maximum and conduction band minimum of our models, it impacts the vibrational frequencies and oscillator strengths (IR intensities) of individual $C(sp^2)$–$C(sp^2)$ stretches, $C(sp^2)$–$C(sp^2)$–$C(sp^2)$ bends, and C–O stretches that contribute to computed IR bands, thus leading to shifts in IR peaks (Figure S29). Together, our results highlight that the composition of the bulk atomic disorder modulates field-dependent IR activity.

## Conclusions

Together, our combined experimental and theoretical work reveals that the bulk of disordered graphitic carbon electrodes exhibit electric-field dependent IR activities, i.e., vibrational Stark effects, that are sensitive to the extent of *bulk* mesoscopic intrinsic disorder. Specifically, the linear relationship between the electric field and electrode potential enables us to draw parallels between experiment and theory. *In-situ* ATR-IR experiments of rGO show blue- and redshifts at 1585 $cm^{-1}$ and 1269 $cm^{-1}$ with decreasing applied potential, respectively. Computationally simulated rGO models show IR peaks in the spectral region consistent with the experiments and blue- and redshifts at 1598 $cm^{-1}$ and 1224 $cm^{-1}$ with decreasing electric fields, respectively. The former band is in line with complex displacements along $C(sp^2)$–$C(sp^2)$ bonds in graphitic domains that disappear with a decrease in the layered graphitic structure and $sp^2$ carbon content. The latter band is in line with complex displacements attributed to $C(sp^2)$–$C(sp^2)$ bonds (i.e., stretching) and $C(sp^2)$–$C(sp^2)$–$C(sp^2)$ angles (i.e., bending) of disordered regions and C–O stretches of the oxidic

defects that persist with a decrease in the $sp^2$ content and layered graphitic structure. First principles simulations suggest that the blue- and redshifts arise from two different mechanisms: the former from changes in the vibrational frequency of the modes from which the band originate, and the other from a change in the relative intensity of the vibrational modes contributing to the band, resulting in an effective shift of the position of the band maximum.

Our work shows that disorder in graphitic carbon electrodes encompasses not only well-defined defects, such as phenolic and ether oxidic moieties but also amorphous regions. These results implicate that materials synthesis strategies to engineer well-defined defects in carbon materials for electrochemical applications must consider their structural consequences on the short- and medium-range order. Our combined spectroelectrochemical and theoretical approach provides a roadmap for identifying mesoscopic disorder in bulk carbon materials, enabling the elucidation of the relationship between this disorder and electrochemical responses.

## Supporting Information

The authors have cited additional references within the Supporting Information.[71–95]

# Research Article

## Conflict of Interest

The authors declare no conflict of interest.

## Data Availability Statement

The data that support the findings of this study are available in the supplementary material of this article.

[1] R. L. McCreery, *Chem. Rev.* **2008**, *108*, 2646–2687.

[2] J. Zhu, S. Mu, *Adv. Funct. Mater.* **2020**, *30*, 2001097.

[3] Y. Jia, X. Yao, *Acc. Chem. Res.* **2023**, *56*, 948–958.

[4] Y. Jia, L. Zhang, L. Zhuang, H. Liu, X. Yan, X. Wang, J. Liu, J. Wang, Y. Zheng, Z. Xiao, E. Taran, J. Chen, D. Yang, Z. Zhu, S. Wang, L. Dai, X. Yao, *Nat. Catal.* **2019**, *2*, 688–695.

[5] X. Wang, Y. Jia, X. Mao, L. Zhang, D. Liu, L. Song, X. Yan, J. Chen, D. Yang, J. Zhou, K. Wang, A. Du, X. Yao, *Chem.* **2020**, *6*, 2009–2023.

[6] A. Shen, Y. Zou, Q. Wang, R. A. W. Dryfe, X. Huang, S. Dou, L. Dai, S. Wang, *Angew. Chem. Int. Ed.* **2014**, *53*, 10804–10808.

[7] L. Zhang, Q. Xu, J. Niu, Z. Xia, *Phys. Chem. Chem. Phys.* **2015**, *17*, 16733–16743.

[8] Y. Jiang, L. Yang, T. Sun, J. Zhao, Z. Lyu, O. Zhuo, X. Wang, Q. Wu, J. Ma, Z. Hu, *ACS Catal.* **2015**, *5*, 6707–6712.

[9] Z. Lu, G. Chen, S. Siahrostami, Z. Chen, K. Liu, J. Xie, L. Liao, T. Wu, D. Lin, Y. Liu, T. F. Jaramillo, J. K. Nørskov, Y. Cui, *Nat. Catal.* **2018**, *1*, 156–162.

[10] J. S. Lim, J. H. Kim, J. Woo, D. S. Baek, K. Ihm, T. J. Shin, Y. J. Sa, S. H. Joo, *Chem.* **2021**, *7*, 3114–3130.

[11] X. Yan, Y. Jia, X. Yao, *Chem. Soc. Rev.* **2018**, *47*, 7628–7658.

[12] W. Wang, L. Shang, G. Chang, C. Yan, R. Shi, Y. Zhao, G. I. N. Waterhouse, D. Yang, T. Zhang, *Adv. Mater.* **2019**, *31*, 1808276.

[13] D. Xue, H. Xia, W. Yan, J. Zhang, S. Mu, *Nano-Micro Lett.* **2021**, *13*, 5.

[14] J. C. Meyer, C. Kisielowski, R. Erni, M. D. Rossell, M. F. Crommie, A. Zettl, *Nano Lett.* **2008**, *8*, 3582–3586.

[15] C. Gómez-Navarro, J. C. Meyer, R. S. Sundaram, A. Chuvilin, S. Kurasch, M. Burghard, K. Kern, U. Kaiser, *Nano Lett.* **2010**, *10*, 1144–1148.

[16] K. Erickson, R. Erni, Z. Lee, N. Alem, W. Gannett, A. Zettl, *Adv. Mater.* **2010**, *22*, 4467–4472.

[17] F. Tuinstra, J. L. Koenig, *J. Chem. Phys.* **1970**, *53*, 1126–1130.

[18] A. Ferrari, J. Robertson, *Phys. Rev. B* **2000**, *61*, 14095.

[19] A. C. Ferrari, *Solid State Commun.* **2007**, *143*, 47–57.

[20] D. S. Knight, W. B. White, *J. Mater. Res.* **1989**, *4*, 385–393.

[21] P. Lespade, R. Al-Jishi, M. S. Dresselhaus, *Carbon* **1982**, *20*, 427–431.

[22] M. J. Matthews, M. A. Pimenta, G. Dresselhaus, M. S. Dresselhaus, M. Endo, *Phys. Rev. B* **1999**, *59*, R6585.

[23] R. Bowling, R. T. Packard, R. L. McCreery, *Langmuir* **1989**, *5*, 683–688.

[24] Z. Xia, V. Bellani, J. Sun, V. Palermo, *Faraday Discuss.* **2021**, *227*, 291–305.

[25] D. C. Alsmeyer, R. L. McCreery, *Anal. Chem.* **1992**, *64*, 1528–1533.

[26] H. Nakagawa, Y. Domi, T. Doi, M. Ochida, S. Tsubouchi, T. Yamanaka, T. Abe, Z. Ogumi, *J. Power Sources* **2013**, *236*, 138–144.

[27] M. S. Jagadeesh, G. Bussetti, A. Calloni, R. Yivlialin, L. Brambilla, A. Accogli, E. Gibertini, D. Alliata, C. Goletti, F. Ciccacci, L. Magagnin, C. Castiglioni, L. Duò, *J. Phys. Chem. C* **2019**, *123*, 1790–1797.

[28] A. A. Papaderakis, A. Ejigu, J. Yang, A. Elgendy, B. Radha, A. Keerthi, A. Juel, R. A. W. Dryfe, *J. Am. Chem. Soc.* **2023**, *145*, 8007–8020.

[29] R. J. Nemanich, G. Lucovsky, S. A. Solin, *Solid State Commun.* **1977**, *23*, 117–120.

[30] G. S. Jeon, G. D. Mahan, *Phys. Rev. B* **2005**, *71*, 184306.

[31] M. Manzardo, E. Cappelluti, E. Van Heumen, A. B. Kuzmenko, *Phys. Rev. B* **2012**, *86*, 054302.

[32] E. Fuente, J. A. Menéndez, M. A. Díez, D. Suárez, M. A. Montes-Morán, *J. Phys. Chem. B* **2003**, *107*, 6350–6359.

[33] M. Acik, G. Lee, C. Mattevi, M. Chhowalla, K. Cho, Y. J. Chabal, *Nat. Mater.* **2010**, *9*, 840–845.

[34] M. Acik, G. Lee, C. Mattevi, A. Pirkle, R. M. Wallace, M. Chhowalla, K. Cho, Y. Chabal, *J. Phys. Chem. C* **2011**, *115*, 19761–19781.

[35] C. Zhang, D. M. Dabbs, L. M. Liu, I. A. Aksay, R. Car, A. Selloni, *J. Phys. Chem. C* **2015**, *119*, 18167–18176.

[36] Z. F. Su, J. Quintal, M. Al-Jeda, A. R. Thiruppathi, J. Lipkowski, A. Chen, *J. Phys. Chem. C* **2023**, *127*, 21644–21655.

[37] S. Y. Toh, K. S. Loh, S. K. Kamarudin, W. R. W. Daud, *Chem. Eng. J.* **2014**, *251*, 422–434.

[38] Y. Yamada, H. Yasuda, K. Murota, M. Nakamura, T. Sodesawa, S. Sato, *J. Mater. Sci.* **2013**, *48*, 8171–8198.

[39] R. Al-Gaashani, A. Najjar, Y. Zakaria, S. Mansour, M. A. Atieh, *Ceram. Int.* **2019**, *45*, 14439–14448.

[40] S. Yumitori, *J. Mater. Sci.* **2000**, *35*, 139–146.

[41] N. Bernier, F. Bocquet, A. Allouche, W. Saikaly, C. Brosset, J. Thibault, A. Charaï, *J. Electron Spectrosc. Relat. Phenom.* **2008**, *164*, 34–43.

[42] D. D'Angelo, C. Bongiorno, M. Amato, I. Deretzis, A. La Magna, E. Fazio, S. Scalese, *J. Phys. Chem. C* **2017**, *121*, 5408–5414.

[43] S. Perumbilavil, P. Sankar, T. Priya Rose, R. Philip, *Appl. Phys. Lett.* **2015**, *107*, 51104.

[44] M. A. Pimenta, G. Dresselhaus, M. S. Dresselhaus, L. G. Cançado, A. Jorio, R. Saito, *Phys. Chem. Chem. Phys.* **2007**, *9*, 1276–1290.

[45] L. G. Cançado, A. Jorio, E. H. M. Ferreira, F. Stavale, C. A. Achete, R. B. Capaz, M. V. O. Moutinho, A. Lombardo, T. S. Kulmala, A. C. Ferrari, *Nano Lett.* **2011**, *11*, 3190–3196.

[46] A. Y. Lee, K. Yang, N. D. Anh, C. Park, S. M. Lee, T. G. Lee, M. S. Jeong, *Appl. Surf. Sci.* **2021**, *536*, 147990.

[47] D. C. Marcano, D. V. Kosynkin, J. M. Berlin, A. Sinitskii, Z. Sun, A. Slesarev, L. B. Alemany, W. Lu, J. M. Tour, *ACS Nano* **2010**, *4*, 4806–4814.

[48] M. Koshino, T. Ando, *Solid State Commun.* **2009**, *149*, 1123–1127.

[49] P. H. Tan, W. P. Han, W. J. Zhao, Z. H. Wu, K. Chang, H. Wang, Y. F. Wang, N. Bonini, N. Marzari, N. Pugno, G. Savini, A. Lombardo, A. C. Ferrari, *Nat. Mater.* **2012**, *11*, 294–300.

[50] H. Ö. Doğan, D. Ekinci, Ü. Demir, *Surf. Sci.* **2013**, *611*, 54–59.

[51] Q. Pan, C. C. Chung, N. He, J. L. Jones, W. Gao, *J. Phys. Chem. C* **2016**, *120*, 14984–14990.

[52] M. Osawa, K. Ataka, K. Yoshii, T. Yotsuyanagi, *J. Electron Spectrosc. Relat. Phenom.* **1993**, *64* (65), 371–379.

[53] M. Osawa, *Bull. Chem. Soc. Jpn.* **1997**, *70*, 2861–2880.

[54] M. Osawa, in *Diffraction and Spectroscopic Methods in Electrochemistry (Advances in Electrochemical Science and Engineering, Vol. 9)* (Eds.: R. C. Alkire, D. M. Kolb, J. Lipkowski, P. N. Ross), Wiley-VCH, New York, **2006**, pp. 269–314.

[55] X. Yang, Z. Sun, T. Low, H. Hu, X. Guo, F. J. García de Abajo, P. Avouris, Q. Dai, *Adv. Mater.* **2018**, *30*, 1704896.

[56] K. Ataka, T. Yotsuyanagi, M. Osawa, *J. Phys. Chem.* **1996**, *100*, 10664–10672.

[57] K.-I. Ataka, M. Osawa, *Langmuir* **1998**, *14*, 951–959.

[58] M. Osawa, M. Tsushima, H. Mogami, G. Samjeské, A. Yamakata, *J. Phys. Chem. C* **2008**, *112*, 4248–4256.

[59] T. Seki, K. Y. Chiang, C. C. Yu, X. Yu, M. Okuno, J. Hunger, Y. Nagata, M. Bonn, *J. Phys. Chem. Lett.* **2020**, *11*, 8459–8469.

[60] D. Enders, T. Nagao, T. Nakayama, M. Aono, *Langmuir* **2007**, *23*, 6119–6125.

[61] J. P. Perdew, A. Zunger, *Phys. Rev. B* **1981**, *23*, 5048–5079.

[62] J. P. Perdew, K. Burke, M. Ernzerhof, *Phys. Rev. Lett.* **1996**, *77*, 3865–3868.

[63] J. P. Perdew, K. Burke, M. Ernzerhof, *Phys. Rev. Lett.* **1997**, *78*, 1396.

[64] F. Gygi, *IBM J. Res. Dev.* **2008**, *52*, 137–144.

[65] D. Yin, N. Lu, Z. Li, J. Yang, *J. Chem. Phys.* **2013**, *139*, 84704.

[66] F. Risplendi, M. Bernardi, G. Cicero, J. C. Grossman, *Appl. Phys. Lett.* **2014**, *105*, 043903.

[67] A. Kundu, Y. Song, G. Galli, *Proc. Nat. Acad. Sci.* **2022**, *119*, e2203083119.

[68] I. Souza, J. Íñiguez, D. Vanderbilt, *Phys. Rev. Lett.* **2002**, *89*, 117602.

[69] Z. Ye, F. Gygi, G. Galli, *J. Phys. Chem. Lett.* **2024**, *15*, 51–58.

[70] S. R. Ryu, I. Noda, Y. M. Jung, *Appl. Spectrosc.* **2010**, *64*, 1017–1021.

[71] M. Osawa, M. Ikeda, *J. Phys. Chem.* **1991**, *95*, 9914–9919.

[72] J. W. Medernach, in *Handbook of Vibrational Spectroscopy* (Ed.: P. R. Griffiths), Wiley, **2001**.

[73] C. Vigano, J. Ruysschaert, E. Goormaghtigh, *Talanta* **2005**, *65*, 1132–1142.

[74] G. Samjeské, A. Miki, S. Ye, M. Osawa, *J. Phys. Chem. B* **2006**, *110*, 16559–16566.

[75] G. Samjeské, A. Miki, M. Osawa, *J. Phys. Chem. C* **2007**, *111*, 15074–15083.

[76] M. Osawa, in *In-Situ Spectroscopic Studies of Adsorption at the Electrode and Electrocatalysis*, Elsevier, **2007**, pp. 209–246.

[77] H. Miyake, T. Okada, G. Samjeské, M. Osawa, *Phys. Chem. Chem. Phys.* **2008**, *10*, 3662.

[78] E. Karabudak, E. Yüce, S. Schlautmann, O. Hansen, G. Mul, H. (J. G. E.) Gardeniers, *Phys. Chem. Chem. Phys.* **2012**, *14*, 10882.

[79] B. Konkena, S. Vasudevan, *J. Phys. Chem. Lett.* **2012**, *3*, 867–872.

[80] N. A. Spaldin, *J. Solid State Chem.* **2012**, *195*, 2–10.

[81] H. Huang, Z. Li, J. She, W. Wang, *J. Appl. Phys.* **2012**, *111*, 054317.

[82] N. Marzari, A. A. Mostofi, J. R. Yates, I. Souza, D. Vanderbilt, *Rev. Mod. Phys.* **2012**, *84*, 1419–1475.

[83] P. Norman, K. Ruud, T. Saue, *Principles and Practices of Molecular Properties: Theory, Modeling, and Simulations.*, John Wiley & Sons Ltd, **2018**.

[84] D. Joung, S. I. Khondaker, *J. Phys. Chem. C* **2013**, *117*, 26776–26782.

[85] H. Ö. Doğan, D. Ekinci, Ü. Demir, *Surf. Sci.* **2013**, *611*, 54–59.

[86] G. Piccini, J. Sauer, *J. Chem. Theory Comput.* **2013**, *9*, 5038–5045.

[87] M. Schlipf, F. Gygi, *Comput. Phys. Commun.* **2015**, *196*, 36–44.

[88] M. Yaguchi, T. Uchida, K. Motobayashi, M. Osawa, *J. Phys. Chem. Lett.* **2016**, *7*, 3097–3102.

[89] A. Kundu, G. Piccini, K. Sillar, J. Sauer, *J. Am. Chem. Soc.* **2016**, *138*, 14047–14056.

[90] E. S. Orth, J. G. L. Ferreira, J. E. S. Fonsaca, S. F. Blaskievicz, S. H. Domingues, A. Dasgupta, M. Terrones, A. J. G. Zarbin, *J. Colloid Interface Sci.* **2016**, *467*, 239–244.

[91] E. Toral-Sánchez, J. A. Ascacio Valdés, C. N. Aguilar, F. J. Cervantes, J. R. Rangel-Mendez, *Carbon* **2016**, *99*, 456–465.

[92] B. Li, S.-X. Chen, A.-L. Li, C. Zexing Wang, J. Prashanth, J. Kishan Ojha, B. Venkatram Reddy, G. Ramana Rao, *J. Phys. Conf. Ser.* **2016**, *759*, 012057.

[93] A. Kundu, M. Govoni, H. Yang, M. Ceriotti, F. Gygi, G. Galli, *Phys. Rev. Mater.* **2021**, *5*, L070801.

[94] A. Wuttig, J. Ryu, Y. Surendranath, *J. Phys. Chem. C* **2021**, *125*, 17042–17050.

[95] A. Kundu, G. Galli, *J. Chem. Theory Comput.* **2023**, *19*, 4011–4022.

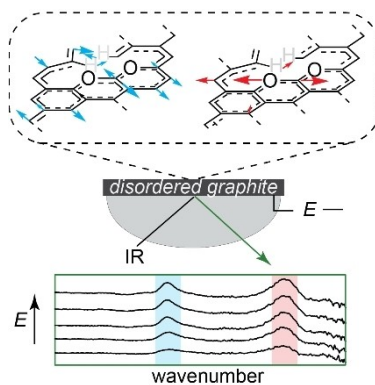## Research Article

*Carbon Electrodes*

R. Papadopoulos, B. Masters, A. Kundu,
N. Maldonado, A. S. Filatov, Y. Liu, T. Kim,
G. Galli, A. Wuttig* ——— e202420680

Unlocking Mesoscopic Disorder in Graph-
itic Carbon with Spectroelectrochemistry

We show that graphitic carbon electro-
des exhibit electric-field dependent infra-
red activity that is sensitive to the bulk
mesoscopic intrinsic disorder. Our com-
bined experimental and theoretical work
provides a roadmap for elucidating
mesoscopic disorder in graphitic carbon
electrode materials under potential bias.